

Order-disorder charge density wave instability in the kagome metal (Cs,Rb)V₃Sb₅

Received: 31 August 2022

Accepted: 6 February 2023

Published online: 23 February 2023

Check for updates

D. Subires¹, A. Korshunov², A. H. Said³, L. Sánchez¹, Brenden R. Ortiz⁴, Stephen D. Wilson⁴, A. Bosak² & S. Blanco-Canosa^{1,5} ✉

The origin of the charge density wave phases in the kagome metal compound AV₃Sb₅ is still under great scrutiny. Here, we combine diffuse and inelastic x-ray scattering to identify a 3-dimensional precursor of the charge order at the *L* point that condenses into a CDW through a first order phase transition. The quasi-elastic critical scattering indicates that the dominant contribution to the diffuse precursor is the elastic central peak without phonon softening. However, the inelastic spectra show a small broadening of the Einstein-type phonon mode on approaching T_{CDW} . Our results point to the situation where the Fermi surface instability at the *L* point is of order-disorder type with critical growth of quasi-static domains. The experimental data indicate that the CDW consists on an alternating Star of David and trihexagonal distortions and its dynamics goes beyond the classical weak-coupling scenario and is discussed within strong-electron phonon coupling and non-adiabatic models.

The intricate relationship between lattice geometry and topological electronic behavior determines the ground state properties of materials. The non-trivial band topology of the kagome lattice is being extensively explored as candidates to engineer Dirac fermions¹, topological flat bands², magnetic Weyl semimetals³ or quantum spin liquid behavior^{4,5}. Besides, the combination between the non-trivial topology and strong electronic correlations, originated from the interplay of orbital, charge and spin degrees of freedom, introduces topological correlated physics⁶ with more exotic phenomena, like topological Majorana modes.

Recently, a new family of non magnetic kagome metals AV₃Sb₅ (A=K, Rb, Cs) has emerged as a fertile playground to investigate correlation-driven topological phases^{7–9}. Derived from the kagome structure, this family of materials features a quasi 2D electronic band structure with van Hove singularities (vHs) and Dirac crossings close to the Fermi level^{10,11}. Superconductivity sets in at low temperature and is intertwined with an exotic charge density wave phase (CDW)¹². Although the electronic structure obtained from density functional theory (DFT) calculations is well established, controversy surrounds

the origin and stabilization of the CDW, and the mechanism of superconductivity and its gap symmetry^{13–15}.

The rich phase diagram of the kagome lattice was investigated with respect to Fermi surface instabilities within the Hubbard model, revealing spin and CDW orders and unconventional superconductivity emerging upon tuning the band filling to the vHs^{16,17}. Diffraction experiments and scanning tunneling microscopy (STM) unraveled multiple-*q* CDW modulations with an inverse Star of David structure (SoD) and a trihexagonal (TrH) distortions^{18,19}, following the phonon instabilities at the *M* and *L* points predicted by DFT^{14,20}. The *q* vector at *M* connects neighbouring vHs in the vicinity of the Fermi surface of AV₃Sb₅, suggesting that the CDW is triggered by the Peierls mechanism^{10,11}. On the other hand, the CDW of CsV₃Sb₅ has been shown to break the time reversal symmetry²¹, unveiling an entanglement of superconductivity and charge order chirality¹⁹. Nevertheless, the chiral CDW has been questioned by recent STM experiments²², pointing to a sample/surface dependent fermiology or the presence of dynamical disorder. This is particularly appealing, since the sample quality and A-site occupancy has a strong impact on the T_c ⁹ and might

¹Donostia International Physics Center (DIPC), San Sebastián, Spain. ²European Synchrotron Radiation Facility (ESRF), BP 220, F-38043 Grenoble Cedex, France. ³Advanced Photon Source, Argonne National Laboratory, Lemont, IL 60439, USA. ⁴Materials Department and California Nanosystems Institute, university of California Santa Barbara, Santa Barbara, CA 93106, USA. ⁵IKERBASQUE, Basque Foundation for Science, 48013 Bilbao, Spain.

✉ e-mail: sblanco@dipc.org

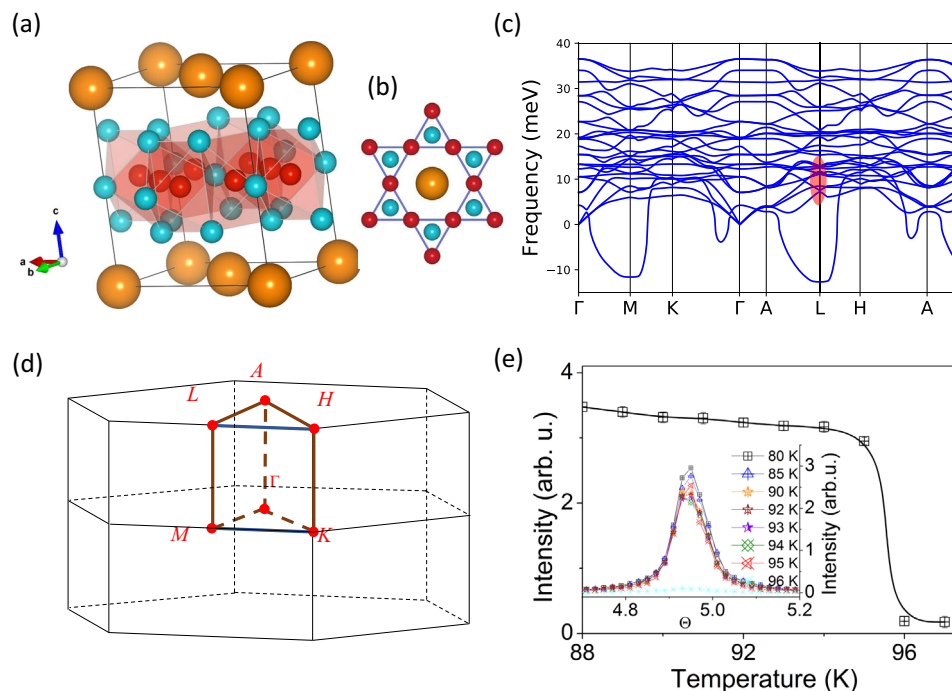


Fig. 1 | Charge density wave in CsV₃Sb₅. **a** Chemical structure of AV₃Sb₅. Orange, red and cyan balls stand for A (Cs, Rb), V and Sb atoms. **b** Top view of the kagome structure, showing the V-kagome net interlaced with the Sb atoms. **c** Calculated phonon dispersions of fully-relaxed CsV₃Sb₅. Soft modes are observed at *M* and *L*.

The red ellipse marks the region where phonons are measured in Fig. 4d. **d** Sketch of the Brillouin zone along the main symmetry directions. **e** Temperature dependence of the (2.5 0.5 0.5) CDW reflection in CsV₃Sb₅, showing a sharp drop of intensity at the $T_{CDW} = 95$ K. (Inset, rocking scans).

also influence the possible origin and stabilization of the charge modulations. Further, recent experiments reported a new unidirectional modulation charge stripe order with $4a_0$ wavelength that breaks the rotational symmetry²², nematicity²³ and pair density wave order²⁴.

Central to the interplay between CDW and \mathbb{Z}_2 band topology is the nature of the CDW phase. From the thermodynamic point of view, specific heat measurements^{8,9} show a small release of entropy through the CDW transition, suggesting a first order phase transition, and tight binding models describe the CDW as electronically mediated^{25,26}. In contrast, DFT predicts soft modes at *M* and *L* points of the Brillouin zone¹⁴, for which, however, inelastic x-ray scattering (IXS) does not observe any anomaly of the low energy acoustic branches²⁷. However, ARPES data have reported deviations from the linear electronic dispersion²⁸, providing that the electron-phonon coupling gives sufficient strength for the CDW formation. Furthermore, optical spectroscopy ascribed the opening of the CDW gap to the suppression of density of states at the *M* point²⁹ with strong phonon renormalizations³⁰ without electronic anomalies at *L*. Finally, in addition to the enigmatic driving force of the CDW, the multiple q_{CDW} and the different energy scales³¹ hinder a detailed study of the ground state of AV₃Sb₅, and the origin and stabilization of the CDW phase transition remains unclear.

Here, we use a combination of diffuse scattering (DS) and inelastic x-ray scattering (IXS) to identify frozen phonon fluctuations of the $2 \times 2 \times 2$ (*L* point) 3D-CDW in AV₃Sb₅ at $T > T_{CDW}$ that condense into a triple- Q_L CDW through a first order phase transition, preserving the six-fold symmetry of the kagome lattice. The precursor of the charge order is absent for the 2×2 (*M* point) and $2 \times 2 \times 4$ superstructures, indicating that the $2 \times 2 \times 2$ charge modulation is the leading Fermi surface instability. Furthermore, the intensity of the quasi-elastic central peak (CP) of IXS follows the diffuse scattering (DS) intensity, showing that the CDW is of an order-disorder transformation type. This is corroborated by the absence of a clear softening, but small broadening of the optical branch at *L*. Our results solve the dispute about the primary order parameter and highlight the critical role of the

order-disorder phase transition to understand the controversial experimental reports.

Results

x-ray diffraction

Figure 1a and b sketches the structure of CsV₃Sb₅ (*P6/mmm* space group). The unit cell is described as individual sublattices of a kagome network of V coordinated by Sb1 atoms and a hexagonal net of Sb2 above and below each kagome layer. The lattice parameters obtained from the DS at room temperature ($a = b = 5.49$ Å, $c = 9.34$ Å) are consistent with the reports in the literature^{7,8}. The temperature dependence of the CDW instability at the *L* point is displayed in the Fig. 1e, showing a sharp onset at -95 K, indicative of a first order-like phase transition. Bragg reflections with the same temperature dependence (not shown) were also measured with propagation vectors (0.5 0 0) and (0.5 0 0.25) r.l.u.²⁷.

Diffuse Scattering, DS

Besides the sharp and intense CDW diffraction spots in x-ray diffraction, diffuse intensity is present at $T > T_{CDW}$ due to lattice vibrations and correlated disorder. Figure 2 summarizes the processed DS maps for the CsV₃Sb₅ sample at 90 and 100 K for the ($h k 0.5$), ($h k 0$) and ($h 0 l$) planes. The image reconstruction of the ($h k 0.5$) plane at 100 K (Fig. 2a, bottom) reveals the presence of DS corresponding to freezing of a transverse component of phonons (streaks highlighted in the yellow square), with most pronounced intensity around the (3 0 0.5) reciprocal lattice vector. Other satellites are equivalent according to the symmetry operations of the *P6/mmm* space group. The DS is visible below 150 K and condense into a $3Q_L$ order at T_{CDW} (Fig. 2a, top). The fluctuating precursor observed in Fig. 2a along the $\langle 1 0 1 \rangle$ direction is in agreement with the phonon calculations that predict a lattice instability at the *L* point, Fig. 1c^{14,20}. The correlation length of the charge precursor (ξ) perpendicular to the streak of diffuse intensity remains nearly constant as we cool down to T_{CDW} and extends to 4-5 unit cells, while along the streak reduces to less than one unit cell, Fig. 3b.

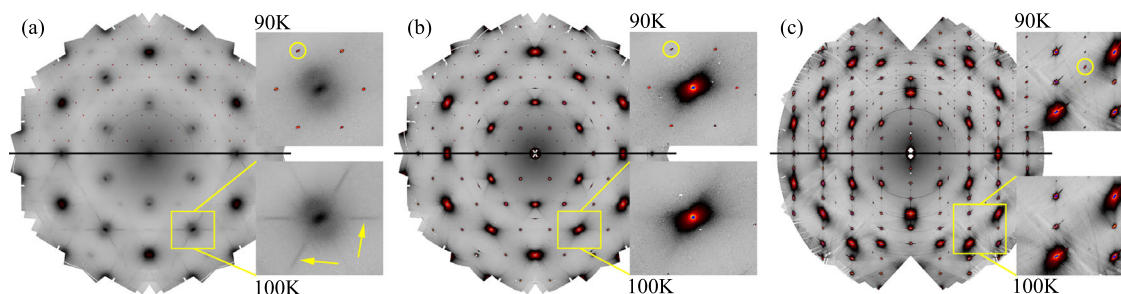


Fig. 2 | Diffuse scattering maps of CsV₃Sb₅. **a** ($hk0.5$) plane at 90 K (top), showing the CDW reflections (weak spots highlighted within the yellow circle in the zoomed in area) and the precursor of the 3D CDW at 100 K (bottom), marked with arrows.

b, c ($hk0$) and ($h0l$) planes, respectively (no precursor). The DS maps of RbV₃Sb₅ are shown in the Supplementary Fig. 1.

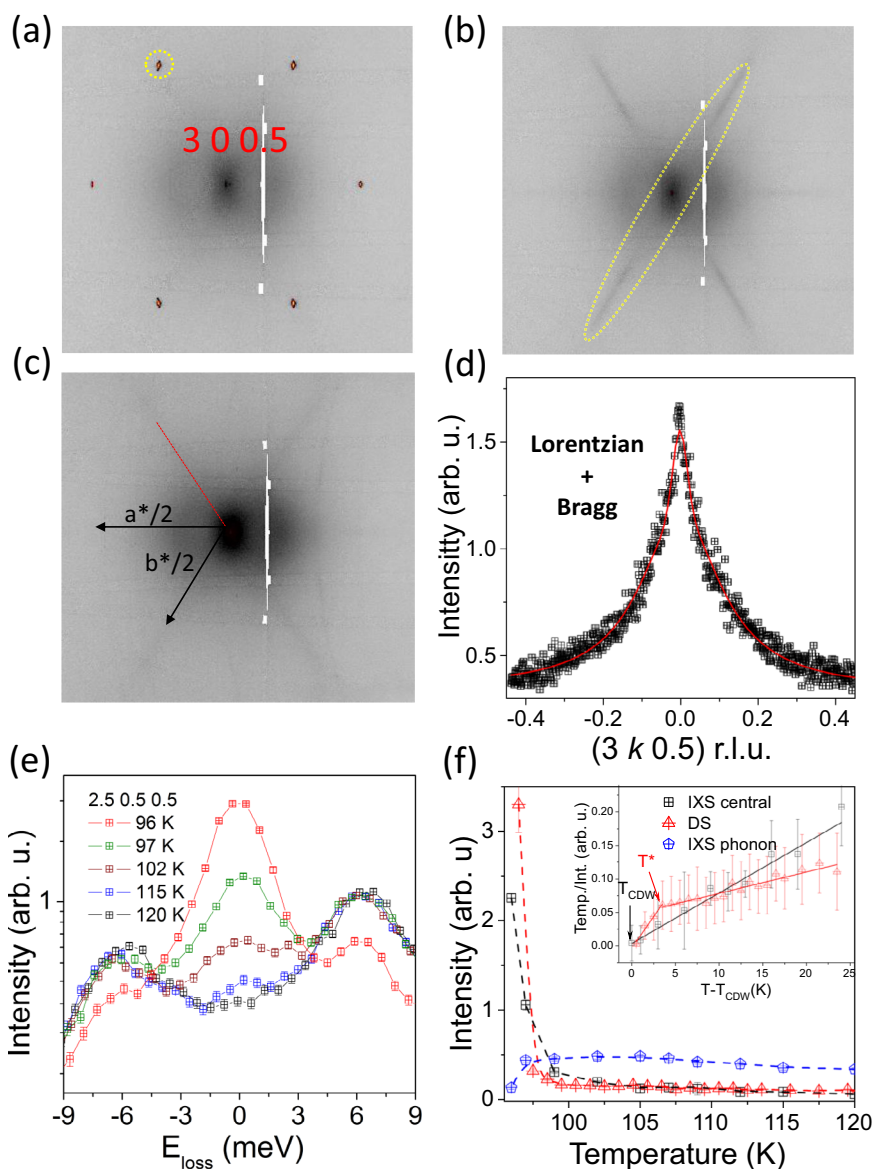


Fig. 3 | Temperature dependence of the diffuse scattering and IXS central peak. **a** 90 K, **b** 100 K and **c** 150 K around the $(3\ 0\ 0.5)$ cut. The sketch in **c** shows the reciprocal lattice vectors and the IXS scan direction through the CDW, as indicated in the red line. **d** Profile of the diffuse scattering at 120 K and its fitting to a sum of Bragg and Lorentzian profiles. **e** Temperature dependence of the IXS spectra at the $(2.5\ 0.5\ 0.5)$ reciprocal lattice vector, highlighting the enhancement of the elastic

line and drop of intensity of the low-energy phonon at 96 K. **f** Temperature dependence of the intensity of the DS signal, elastic central peak and optical phonon. Inset, temperature dependence of the generalized susceptibility. T^* denotes the change of slope of the electronic susceptibility, -105 K, presumably related to percolation of CDW domains. The error bars are the fit to uncertainty.

Remarkably, DS is absent for $T > T_{CDW}$ in the $(h\ k\ 0)$ plane (Fig. 2b, bottom) and $(h\ 0\ l)$ plane (Fig. 2c, bottom) that maps the longitudinal component of the $(0.5\ 0\ 0.25)$ and $(0.5\ 0\ 0.5)$ CDWs^{19,22,27}. However, CDW reflections are again present at $T < T_{CDW}$, matching the hard x-ray diffraction data of Fig. 1e. The presence of diffuse intensity as satellites at only the $(0.5\ 0\ 0.5)$ reciprocal lattice vector indicates that the Fermi surface instability at the L position is the leading order parameter and drives the CDW formation in the kagome metal AV_3Sb_5 (see Supplementary Fig. 1 for the DS maps of RbV_3Sb_5).

The reconstruction of the $(h\ k\ 0.5)$ plane for CsV_3Sb_5 at different temperatures around the $(3\ 0\ 0.5)$ cut is shown in Fig. 3a-c. Figure 3d shows the profile of the diffuse precursor along the diffuse streak of the Fig. 3b. The critical scattering was modelled assuming a sum of Bragg and a Lorentzian profile that accounts for the peak sharpening as T approaches T_{CDW} from the high temperature. The temperature dependence of the DS intensity is extracted by integrating the diffuse precursor and plotted in Fig. 3f. It starts at temperatures below 150 K and increases down to 100-105 K, below which it sharply diverges at the critical temperature, following the temperature dependence of the energy integrated experiment of Fig. 1e.

Inelastic x-ray scattering, IXS

To disentangle static and dynamic contributions and to get further insights about the origin of the observed diffuse features, we have carried out IXS scanning the $(2.5\ 0.5\ 0.5)$ satellite. As shown in Fig. 3e, the IXS spectra consists on a (quasi)-elastic central peak (zero energy loss) evolving in intensity below 120 K and a low energy non-dispersive phonon at 6 meV. The intensity of the CP sharply drops upon warming from 95 K and follows the intensity of the pretranslational fluctuations detected by DS above 105 K. The CP of CsV_3Sb_5 shows parallels to the critical scattering observed in $SrTiO_3$ ^{32,33} and transition metal dichalcogenides³⁴ exhibiting a critical divergence on approaching T_{CDW} . On the other hand, directly visualized in the raw data of Fig. 3e, the intensity of the low-energy mode increases smoothly upon cooling and drops below 100 K due to the modification of the dynamic structure factor on approaching the CDW phase, making the quasi-elastic contribution more important than the phonon intensity to the DS. Following the applicability of the Ornstein-Zernike correlation function³⁵, the generalized susceptibility, $\chi(q)$, proportional to the q Fourier component of the displacement-displacement correlation function $\langle |u_q|^2 \rangle = k_B T \chi(q)$, displays a linear Curie-Weiss behavior for the quasi-elastic component of the CP (inset of Fig. 3f) and vanishes at the critical temperature, indicating a temperature dependence of the density of states. Nevertheless, $\chi(q)$ of the DS changes slope at $T^* - 105$ K, coinciding with the drop of intensity of the low-energy phonon and the deviation of the DS and CP intensities (we tentatively associate T^* as the temperature where the CDW domains start to percolate).

Focusing on the inelastic part of the IXS spectra, Fig. 4a shows the momentum dependence of the phonon dispersion along the $(h\ h\ 0.5)$ direction ($\Delta E=3$ meV). The spectra consist on 3 weakly dispersive branches with 2.5 (γ), 6 (ω) and 11 meV (δ) at $h=0$. The lowest energy mode merges with the 6 meV branch at 0.1 r.l.u. and, at the L point, only two optical-like modes, ω and δ , are observed. These two modes are better visualized in Fig. 4b and its energy dispersion, obtained from the fitting to damped harmonic oscillators (DHO) convoluted with the experimental resolution, is displayed in the Fig. 4c. They exhibit a weak dispersion in reciprocal space and can be described as a system of independent quantum oscillators or localized atomic vibrations (Einstein-type phonon modes). To isolate the contribution of each mode, we increased the energy resolution down to 1.5 meV and work at the $(3.5\ 2.5\ 0.5)$ reciprocal lattice vector. Figure 4d shows the temperature dependence of the ω branch. Indeed, the ω phonon in Fig. 4b consists on 2 modes, which we label here as ω_1 and ω_2 , in good agreement the DFPT calculations in Fig. 1c (Supplementary Fig. 2). From these data, the energy of ω_1 and ω_2 remains constant as the temperature

approaches the CDW transition. This clearly demonstrates the absence of a Kohn anomaly and discards a soft phonon nature of the CDW phase transition; i.e, it is not phonon driven but of order-disorder type. This does not preclude the presence of a soft mode below T_{CDW} , which is, in fact, a fingerprint of both order-disorder and displacive phase transitions. We need to stress here that it is not the crystal quality, but the inherent dynamical disorder that stabilizes the CDW in CsV_3Sb_5 . On the other hand, a detailed analysis of the phonon linewidth reveals an anomalous broadening at T_{CDW} . At 150 K, ω_1 is not resolution limited and develops a small intrinsic broadening of -0.5 meV (a DHO with 0 meV intrinsic width corresponds to the instrumental resolution of 1.5 meV). Upon cooling, the width of the phonon decreases and becomes resolution limited at 105 K. However, its width increases again (not resolution limited) below 100 K, coinciding with T^* , a signature of a proximity to a Fermi surface instability.

Discussion

The results presented here indicate that weak coupling limit theories, $\omega_{2k_f} \tau_{eh} < 1$ (ω_{2k_f} and τ_{eh} are the bare phonon frequency and electron-hole pair lifetime, respectively), are not adequate to interpret the absence of the Kohn anomaly and the major contribution of the CP to diffuse scattering data. This locates the CDW instability of AV_3Sb_5 in the strong coupling non-adiabatic or in the strong electron-phonon interaction (EPI) regimes. Indeed, recent reflectivity measurements have reported a much larger CDW gap than the weak-coupling BCS value^{29,36}. The effect of the dynamical disorder was theoretically modelled by Yu and Anderson³⁷ for the strong interaction of electrons and single dispersionless (Einstein-type) optical modes and further extended by Gor'kov³⁸ for any arbitrary ionic displacements. Within this scenario, the CDW in AV_3Sb_5 realizes in two stages. First, an ionic displacement in the kagome plane introduces a strong EPI that traps the electronic cloud near an ion, changing the local electronic environment and breaking the adiabatic approximation. This gives rise to a quasi-elastic response above the CDW transition, an associated order-disorder dynamics and the absence of a Kohn anomaly. In an order-disorder transformation, the harmonic potential well deforms and the phase transition is achieved by the critical growth and percolation of quasi-static domains on approaching the critical temperature³⁹. In each domain, the potential within the atom moves is quasi-harmonic and phonon anomalies are expected. This naturally explains the change of slope in the *diffuse* susceptibility of Fig. 3f and the small broadening of the low-energy mode in Fig. 4d, e. Strong EPI mechanisms have been considered to explain the CDW formation in the one dimensional Peierls instability of $BaVS_3$ ^{40,41}, transition metal dichalcogenides⁴², H-bond ferroelectrics⁴³ and the controversial charge order in high- T_c cuprates⁴⁴. On the other hand, in the non-adiabatic dynamics, ω_{2k_f} fluctuates so rapidly that cannot couple with the electron-hole condensate during the electron-hole pair lifetime. The rapidly fluctuating phonon reduces the screening between atoms and prevents the development of the Kohn anomaly at T_{CDW} . Following this argument, the suppression of the Peierls transition of $BaVS_3$ under pressure was interpreted as a reduction of the τ_{eh} ⁴⁵. This is a particularly appealing scenario since the T_{CDW} of CsV_3Sb_5 is completely suppressed at low pressures and evolves towards a double superconducting dome⁴⁶⁻⁴⁹.

We would like to finish our discussion by placing our results within the physics of the kagome metals AV_3Sb_5 . The identification of the charge order fluctuations at $T > T_{CDW}$ indicates that the condensation of the CDW order parameter at the L point in $(Cs,Rb)V_3Sb_5$ is the leading instability, favoring the alternating Star of David and trihexagonal (LLL) pattern⁵⁰. The absence of DS at the M point suggests that the strength of the coupling parameter of the L and M modes in the Landau free energy expansion, γ_{ML} , is rather small or the phase transition is more strongly first-order (the condition for the susceptibility at the M point to diverge is $\xi^2 - \gamma_{ML}$, where ξ is the correlation length of

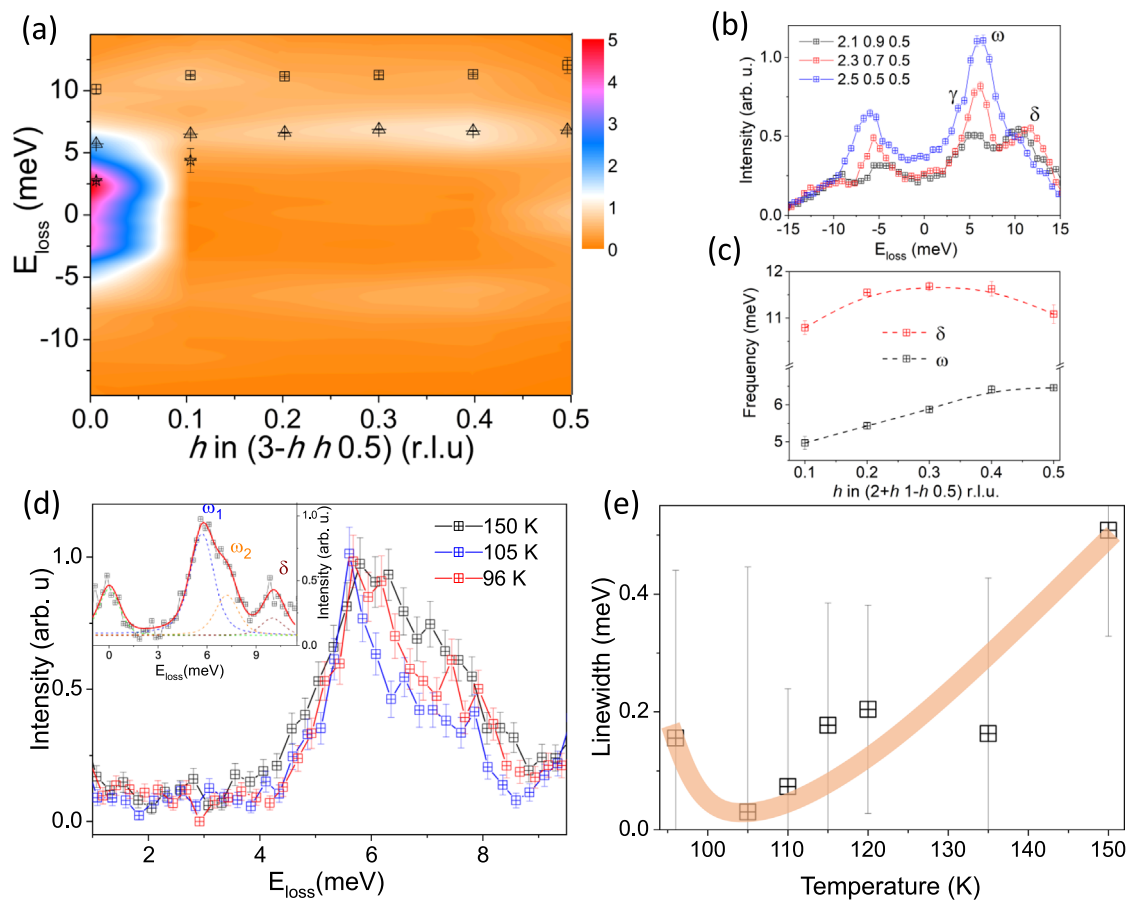


Fig. 4 | Einstein modes and phonon broadening. **a** Color map of the low-energy phonons of CsV₃Sb₅ along the $(3-h \ h \ 0.5)$ direction at 120 K. The three modes identified at 2.5 (γ , asterisks), 6 (ω , triangles) and 11 meV (δ , squares) are superimposed. **b** IXS spectra and **c** dispersion along the $(2+h \ 1-h \ 0.5)$ direction ($\Delta E = 3$ meV) of the δ and ω branches. **d** Temperature dependent high resolution

IXS spectra ($\Delta E = 1.5$ meV) at the 3.5 2.5 0.5 reciprocal lattice vector. Inset, fitting details of the scan at 150 K. Note that, ω in **b** is now resolved as 2 modes, ω_1 and ω_2 . **e** Temperature dependence of the linewidth of ω_1 . The error bars represent the fit uncertainty. See Supplementary for the fitting details and Supplementary Fig. 3.

the L order. If ξ never becomes too large, one would not expect an enhancement of the M susceptibility above T_{CDW} . R. M. Fernandes, *Private Communication*). Our DS results also indicate that the 6-fold symmetry is preserved, discarding single Q_M /double Q_L orders (staggered SoD and staggered TrH). Rather, our data seem to agree with the experiments that support a combination of triple Q_M /triple Q_L order ($LLL+MMM$ pattern)^{51,52} at low temperature.

On the other hand, the importance of the EPI has been highlighted recently by neutron scattering⁵³ and, perhaps, acts concomitantly with nesting to enhance the charge correlations. Coherent phonon spectroscopy reported a condensation of M and L -point phonons, suggesting an order-disorder crossover at lower temperature⁵⁴ to a different ordering pattern as observed here. An order-disorder transition is expected to be of first order type, thus the small release of entropy at T_{CDW} ^{8,9} fits within this scenario. Moreover, the data presented here does not conflict with the possible chiral charge density wave, but put constraints on the nematic order^{22,23}. Broken rotational symmetries can be affected by local dynamic disorder, fluctuating domains and defects that introduce pinning potentials. These pinning centers and local distortions introduce variations of the amplitudes of the local atomic displacements, which can be detected by pair distribution function (PDF) analysis⁵⁵.

In conclusion, we have presented diffuse scattering and inelastic x-ray scattering data to demonstrate that the CDW in the kagome metal AV₃Sb₅ is of order-disorder type without phonon softening. A precursor of the CDW is observed in diffuse scattering with propagation vector $(0.5 \ 0 \ 0.5)$, indicating that the CDW instability at the L point

is the primary order parameter, discarding a broken six-fold rotational symmetry at high temperature and pointing to an LLL pattern. Furthermore, we demonstrate that the diffuse signal contains intensity of the quasi-elastic central peak, likely due to the growth of fluctuating domains, thus favouring strong coupling theories to describe the CDW ground state of AV₃Sb₅. Our results present a step forward and provide crucial information to understand the enigmatic charge order of (Cs,Rb)V₃Sb₅.

Methods

Single crystals of AV₃Sb₅ (A=Cs, Rb) with $T_{CDW}=95$ and 104 K, were synthesized by the self-flux growth method⁷. Diffuse scattering measurements were performed with a Dectris PILATUS3 1M X area detector at the ID28 beamline at the European Synchrotron Research Facility (ESRF) with an incoming energy $E_i=17.8$ keV. Orientation matrix refinement and reciprocal space reconstructions were done using the CrysAlis software package. Final DS images were processed with an in-house code. Low energy phonons were measured by inelastic x-ray scattering (IXS) at the ID28 IXS station at ESRF ($E_i=17.8$ keV, $\Delta E=3$ meV) and at the HERIX beamline at the Argonne Photon Source (APS) ($E_i=23.72$ keV, $\Delta E=1.5$ meV). The components (hkl) of the scattering vector are expressed in reciprocal lattice units (r.l.u.), $(hkl) = h\mathbf{a}^* + k\mathbf{b}^* + l\mathbf{c}^*$, where \mathbf{a}^* , \mathbf{b}^* , and \mathbf{c}^* are the reciprocal lattice vectors.

Lattice dynamic calculations were performed by Density Functional Perturbation Theory (DFPT) as implemented in QUANTUM ESPRESSO package. The forces were calculated in $8 \times 8 \times 4$ supercells using the ultrasoft parametrization of the PBE exchange-correlation

functional. We set the energy cutoffs of 60 and 600 Ry for the basis-set and treated the Van der Waals corrections within the Grimme's semi-empirical approach. An $8 \times 8 \times 4$ k-point grid and a Marzari-Vanderbilt smearing of 0.01 Ry was used for the Brillouin zone integration. The convergence threshold was set to 10^{-19} .

Data availability

All data needed to evaluate the conclusions in the paper are included in the paper and in the Supplementary Information. The DS and IXS data generated in this study have been deposited in the Figshare database <https://doi.org/10.6084/m9.figshare.21990461>.

References

- Ye, L. et al. Massive Dirac fermions in a ferromagnetic kagome metal. *Nature* **555**, 638–642 (2018).
- Kang, M. et al. Dirac fermions and flat bands in the ideal kagome metal FeSn. *Nat. Mater.* **19**, 163–169 (2020).
- Liu, E. et al. Giant anomalous Hall effect in a ferromagnetic kagome-lattice semimetal. *Nat. Phys.* **14**, 1125–1131 (2018).
- Yan, S., Huse, D. & Steven, R. White Spin-Liquid Ground State of the $S = 1/2$ Kagome Heisenberg Antiferromagnet. *Science* **332**, 1173–1176 (2011).
- Han, T. et al. Fractionalized excitations in the spin-liquid state of a kagome-lattice antiferromagnet. *Nature* **492**, 406–410 (2012).
- Mazin, I. et al. Theoretical prediction of a strongly correlated Dirac metal. *Nat. Commun.* **5**, 4261 (2014).
- Ortiz, B. et al. New kagome prototype materials: discovery of KV_3Sb_5 , RbV_3Sb_5 , and CsV_3Sb_5 . *Phys. Rev. Mater.* **3**, 094407 (2019).
- Ortiz, B. et al. CsV_3Sb_5 : A \mathbb{Z}_2 Topological Kagome Metal with a Superconducting Ground State. *Phys. Rev. Lett.* **125**, 247002 (2020).
- Ortiz, B. et al. Superconductivity in the \mathbb{Z}_2 kagome metal KV_3Sb_5 . *Phys. Rev. Mater.* **5**, 034801 (2021).
- Kang, M. et al. Twofold van Hove singularity and origin of charge order in topological kagome superconductor CsV_3Sb_5 . *Nat. Phys.* **18**, 301–308 (2022).
- Lou, R. et al. Charge-Density-Wave-Induced Peak-Dip-Hump Structure and the Multiband Superconductivity in a Kagome Superconductor CsV_3Sb_5 . *Phys. Rev. Lett.* **128**, 036402 (2022).
- Zhao, H. et al. Cascade of correlated electron states in the kagome superconductor CsV_3Sb_5 . *Nature* **599**, 216–221 (2021).
- Zhao, C. et al. Nodal superconductivity and superconducting domes in the topological Kagome metal CsV_3Sb_5 . *ArXiv:2102.08356v2*.
- Tan, H., Liu, Y., Wang, Z. & Yan, B. Charge Density Waves and Electronic Properties of Superconducting Kagome Metals. *Phys. Rev. Lett.* **127**, 046401 (2021).
- Wu, X. et al. Nature of Unconventional Pairing in the Kagome Superconductors AV_3Sb_5 (A=K, Rb, Cs). *Phys. Rev. Lett.* **127**, 177001 (2021).
- Kiesel, M., Platt, C. & Thomale, R. Unconventional Fermi Surface Instabilities in the Kagome Hubbard Model. *Phys. Rev. Lett.* **110**, 126405 (2013).
- Wang, W., Li, Z., Xiang, Y. & Wang, Q. Competing electronic orders on kagome lattices at van Hove filling. *Phys. Rev. B* **87**, 115135 (2013).
- Miao, H. et al. Geometry of the charge density wave in the kagome metal AV_3Sb_5 . *Phys. Rev. B* **104**, 195132 (2021).
- Jiang, Y. et al. Unconventional chiral charge order in kagome superconductor KV_3Sb_5 . *Nat. Mater.* **20**, 1353–1357 (2021).
- Subedi, Alaska Hexagonal-to-base-centered-orthorhombic 4Q charge density wave order in kagome metals KV_3Sb_5 , RbV_3Sb_5 , and CsV_3Sb_5 . *Phys. Rev. Mater.* **16**, 015001 (2022).
- Mielke, C. et al. Time-reversal symmetry-breaking charge order in a kagome superconductor. *Nature* **602**, 245–250 (2022).
- Li, H. et al. Rotation symmetry breaking in the normal state of a kagome superconductor KV_3Sb_5 . *Nat. Phys.* **18**, 265–270 (2022).
- Nie, L. et al. Charge-density-wave-driven electronic nematicity in a kagome superconductor. *Nature* **604**, 59–64 (2022).
- Chen, H. et al. Roton pair density wave in a strong-coupling kagome superconductor. *Nature* **599**, 222–228 (2021).
- Denner, M., Thomale, R. & Neupert, T. Analysis of Charge Order in the Kagome Metal AV_3Sb_5 (A=K, Rb, Cs). *Phys. Rev. Lett.* **127**, 217601 (2021).
- Feng, X., Jiang, K., Wang, Z. & Hu, J. Chiral flux phase in the Kagome superconductor AV_3Sb_5 . *Sci. Bull.* **66**, 1384–1388 (2021).
- Li, H. et al. Observation of Unconventional Charge Density Wave without Acoustic Phonon Anomaly in Kagome Superconductors AV_3Sb_5 (A=Rb, Cs). *Phys. Rev. X* **11**, 031050 (2021).
- Luo, H. et al. Electronic nature of charge density wave and electron-phonon coupling in kagome superconductor KV_3Sb_5 . *Nat. Commun.* **13**, 273 (2022).
- Zhou, X. et al. Origin of charge density wave in the kagome metal CsV_3Sb_5 as revealed by optical spectroscopy. *Phys. Rev. B* **104**, L041101 (2021).
- Uykur, E., Ortiz, B., Wilson, S., Dressel, M. & Tsirlin, A. Optical detection of the density-wave instability in the kagome metal KV_3Sb_5 . *Npj Quantum Mater.* **7**, 16 (2022).
- Nakayama, K. et al. Multiple energy scales and anisotropic energy gap in the charge-density-wave phase of the kagome superconductor CsV_3Sb_5 . *Phys. Rev. B* **104**, L161112 (2021).
- Riste, T., Samuelsen, E., Otnes, K. & Feder, J. Critical behaviour of $SrTiO_3$ near the 105 K phase transition. *Solid State Commun.* **9**, 1455–1458 (1971).
- Shapiro, S., Axe, J., Shirane, G. & Riste, T. Critical Neutron Scattering in $SrTiO_3$ and $KMnF_3$. *Phys. Rev. B* **6**, 4332–4341 (1972).
- Moncton, D., Axe, J. & DiSalvo, F. Neutron scattering study of the charge-density wave transitions in 2H-TaSe₂ and 2H-NbSe₂. *Phys. Rev. B* **16**, 801–819 (1977).
- Rouxel, J. *Crystal Chemistry and Properties of Materials with Quasi-One-Dimensional Structures*. (D. Riedel, Dordrecht, 1986).
- Uykur, E. et al. Low-energy optical properties of the nonmagnetic kagome metal CsV_3Sb_5 . *Phys. Rev. B* **104**, 045130 (2021).
- Yu, C. & Anderson, P. Local-phonon model of strong electron-phonon interactions in A15 compounds and other strong-coupling superconductors. *Phys. Rev. B* **29**, 6165–6186 (1984).
- Gor'kov, L. Strong electron-lattice coupling as the mechanism behind charge density wave transformations in transition-metal dichalcogenides. *Phys. Rev. B* **85**, 165142 (2012).
- Bruce, A. & Cowley, R. A. Structural phase transitions III. Critical dynamics and quasi-elastic scattering. *Adv. Phys.* **29**, 219–321 (1980).
- Ilakovac, V. et al. Order-disorder type of Peierls instability in $BaVS_3$. *Phys. Rev. B* **103**, 014306 (2021).
- Girard, A. et al. Soft-phonon driven hexagonal-orthorhombic phase transition in $BaVS_3$. *Phys. Rev. B* **99**, 144104 (2019).
- Barker, A., Ditzinger, J. & DiSalvo, F. Infrared study of the electronic instabilities in tantalum disulfide and tantalum diselenide. *Phys. Rev. B* **12**, 2049–2054 (1975).
- Blinic, R. & Žekš, B. Dynamics of order-disorder-type ferroelectrics and anti-ferroelectrics. *Adv. Phys.* **21**, 693–757 (1972).
- Le Tacon, M. et al. Inelastic X-ray scattering in $YBa_2Cu_3O_{6.6}$ reveals giant phonon anomalies and elastic central peak due to charge-density-wave formation. *Nat. Phys.* **10**, 52–58 (2014).
- Bernu, S. et al. Vanishing of the metal-insulator Peierls transition in pressurized $BaVS_3$. *Phys. Rev. B* **86**, 235105 (2012).
- Yu, F. et al. Unusual competition of superconductivity and charge-density-wave state in a compressed topological kagome metal. *Nat. Commun.* **12**, 3645 (2021).

47. Zhu, C. et al. Double-dome superconductivity under pressure in the V-based kagome metals AV_3Sb_5 (A=Rb and K). *Phys. Rev. B* **105**, 094507 (2022).
 48. Yu, F. et al. Pressure-Induced Dimensional Crossover in a Kagome Superconductor. *Phys. Rev. Lett.* **128**, 077001 (2022).
 49. Wang, N. et al. Competition between charge-density-wave and superconductivity in the kagome metal RbV_3Sb_5 . *Phys. Rev. Res.* **3**, 043018 (2021).
 50. Christensen, M. H., Birol, T., Andersen, B. M. & Fernandes, R. M. Theory of the charge density wave in AV_3Sb_5 kagome metals. *Phys. Rev. B* **104**, 214513 (2021).
 51. Kang, Mingu et al. Charge order landscape and competition with superconductivity in kagome metals. *Nat. Mater.* **22**, 1–8 (2022).
 52. Luo, H. et al. Electronic nature of charge density wave and electron-phonon coupling in kagome superconductor KV_3Sb_5 . *npj Quantum Mater.* **7**, 30 (2022).
 53. Xie, Yaofeng et al. Electron-phonon coupling in the charge density wave state of CsV_3Sb_5 . *Phys. Rev. B* **105**, L140501 (2022).
 54. Ratcliff, Noah, Hallett, Lily, Ortiz, B. R., Wilson, S. D. & Harter, J. W. Coherent phonon spectroscopy and interlayer modulation of charge density wave order in the kagome metal CsV_3Sb_5 . *Phys. Rev. Mater.* **5**, L111801 (2021).
 55. Upreti, P. et al. Order-Disorder Transitions in $(Ca_xSr_{1-x})_3Rh_4Sn_{13}$. *Phys. Rev. Lett.* **128**, 095701 (2022).
- experiments. D.S., A.K., A.H.S., L.S., A.B. and S.B-C. carried out the IXS measurements. S.B-C. performed the DFPT calculations, analyzed the data and wrote the manuscript with input from all coauthors.

Competing interests

The authors declare no competing interests.

Additional information

Supplementary information The online version contains supplementary material available at <https://doi.org/10.1038/s41467-023-36668-w>.

Correspondence and requests for materials should be addressed to S. Blanco-Canosa.

Peer review information : *Nature Communications* thanks Hu Miao, and the other, anonymous, reviewers for their contribution to the peer review of this work. Peer reviewer reports are available.

Reprints and permissions information is available at <http://www.nature.com/reprints>

Publisher's note Springer Nature remains neutral with regard to jurisdictional claims in published maps and institutional affiliations.

Acknowledgements

We acknowledge E. Efremov, A. Schnyder, A. Bernevig, A. Subedi, J. Diego, L. Elcoro, I. Etxebarria, D. Chernyshov and R. Fernandes for fruitful discussions and critical reading of the manuscript. S.B-C, D.S and L.S thank the MINECO of Spain through the project PGC2018-101334-A-C22. S.D.W and B.R.O gratefully acknowledge support via UC Santa Barbara NSF Quantum Foundry funded via the Q-AMASE-i program under award DMR-1906325. This research used resources of the Advanced Photon Source, a U.S. Department of Energy (DOE) Office of Science user facility operated for the DOE Office of Science by Argonne National Laboratory under Contract No. DE-AC02-06CH11357.

Author contributions

S.B-C. conceived and managed the project. B.O. and S.D.W. synthesized and characterized the samples. A.K., A.B. and S.B-C. performed the DS

Open Access This article is licensed under a Creative Commons Attribution 4.0 International License, which permits use, sharing, adaptation, distribution and reproduction in any medium or format, as long as you give appropriate credit to the original author(s) and the source, provide a link to the Creative Commons license, and indicate if changes were made. The images or other third party material in this article are included in the article's Creative Commons license, unless indicated otherwise in a credit line to the material. If material is not included in the article's Creative Commons license and your intended use is not permitted by statutory regulation or exceeds the permitted use, you will need to obtain permission directly from the copyright holder. To view a copy of this license, visit <http://creativecommons.org/licenses/by/4.0/>.

© The Author(s) 2023